

Article

# Microstructure Formation of Low-Carbon Ferritic Stainless Steel during High Temperature Plastic Deformation

Yi Shao, Xiaohua Li, Junjie Ma, Chenxi Liu \* and Zesheng Yan

State Key Lab of Hydraulic Engineering Simulation and Safety, School of Materials Science & Engineering, Tianjin University, Tianjin 300072, China; shzyshy@163.com (Y.S.); lixh@bohaisteel.com (X.L.); 15002233349@163.com (J.M.); mouselcx@21cn.com (Z.Y.)

\* Correspondence: cxliutju@163.com; Tel.: +86-22-8740-1873

Received: 11 March 2019; Accepted: 18 April 2019; Published: 20 April 2019



**Abstract:** In this paper, the effects of the deformation temperature, the deformation reduction and the deformation rate on the microstructural formation, ferritic and martensitic phase transformation, stress–strain behaviors and micro-hardness in low-carbon ferritic stainless steel were investigated. The increase in deformation temperature promotes the formation of the fine equiaxed dynamic strain-induced transformation ferrite and suppresses the martensitic transformation. The higher deformation temperature results in a lower starting temperature for martensitic transformation. The increase in deformation can effectively promote the transformation of DSIT ferrite, and decrease the martensitic transformation rate, which is caused by the work hardening effect on the metastable austenite. The increase in the deformation rate leads to an increase in the ferrite fraction, because a high density of dislocation remains that can provide sufficient nucleation sites for ferrite transformation. The slow deformation rate results in dynamic recovery according to the stress–strain curve.

**Keywords:** ferritic stainless steel; plastic deformation; dynamic strain-induced transformation

## 1. Introduction

Ferritic stainless steels have been widely used in railway transportation equipment, mining machinery, the auto industry and nuclear fission power plant components, because of their remarkable corrosion resistance, outstanding strength and toughness, good weld ability and high cost performance [1–5]. In particular, low-carbon 11–13% Cr ferritic stainless steels have lower material cost than austenitic stainless steels and high Cr ferritic stainless steels, due to their lower contents of Cr and Ni [6,7]. To maintain the ferritic phase at room temperature, the austenite-stabilization elements C, N, and Ni are strictly controlled at a low level [8,9].

Severe plastic deformation is a practical route for the improvement of mechanical properties in the ferritic stainless steels, since in their case it is difficult to realize the effect of phase transformation strengthening [10]. It has been recognized that ultrafine grain structure can be obtained during severe plastic deformation in ferritic stainless steels [11]. The increase in deformation temperature accelerates the kinetics of ultrafine grain evolution significantly. During hot deformation, dynamic recrystallization and dynamic recovery occur, while dynamically recovered and sub-microstructures can be obtained during warm deformation [12]. The dynamic recrystallization may occur in the coarse-grained structure during severe plastic deformation at ambient temperature [13]. However, due to their restricted ferrite-forming elements, low-carbon ferritic stainless steels may enter the austenite phase regions at high temperature. Thus, the effect of austenitic transformation and the subsequent decomposing of austenite on severe plastic deformation in low-carbon ferritic stainless steels should be considered, though it has been rarely reported until now.

This project focuses on the high temperature plastic deformation in the austenite phase region in a low-carbon ferritic stainless steel. The effects of the deformation temperature, the deformation reduction and the deformation rate on the microstructural formation, ferritic and martensitic phase transformation, stress–strain behaviors and micro-hardness in the low-carbon ferritic stainless steel were studied.

## 2. Experimental Details

The chemical composition of the employed low-carbon ferritic stainless steel is given in Table 1. The chemical compositions of the sample were obtained by inductively coupled plasma optical emission spectrometry (ICP-OES). The original state of the samples was the as-rolled plate, whose rolling parameters were that the rolling passes occurred six times, the total rolling reduction was 80%, and the finishing rolling temperature was about 600 °C. Due to this low finishing temperature during rolling, the dynamic recrystallization process would be incomplete, and thus the as-rolled microstructure remained at room temperature. The microstructure of the as-rolled sample is presented in Figure 1, which shows the typical rolled morphology. The grains are elongated along the rolling direction. Besides, the severe deformation would result in a high density of dislocation, although it cannot be observed in the optical micrograph, due to the low resolution.

**Table 1.** Chemical compositions of the employed low-carbon ferritic stainless steel (wt. %).

C	Cr	Si	Ni	Mn	Nb	Ti	Fe
0.01	11.54	0.2	0.57	1.12	0.09	0.12	Bal.

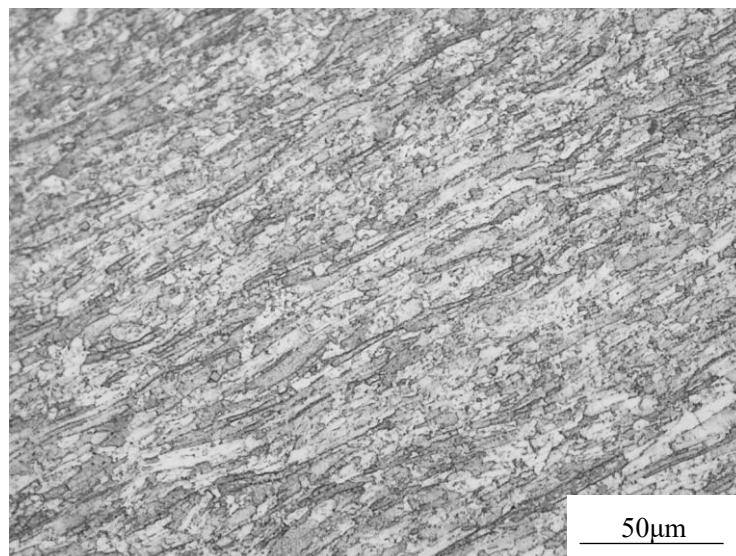


**Figure 1.** The original microstructure of the employed low-carbon ferritic stainless steel.

The deformation experiments were conducted on the Gleeble-3500 thermal simulated test machine (DSI, New York, NY, USA). In this paper, the effect of the deformation temperature, the deformation reduction (referring to the relative deformation in this project, the same as below) and the deformation rate were investigated. The process procedures are illustrated in Figure 2 and Table 2. For the deformation temperature experiments, the samples were heated to 1000 °C and held for 10 min, with a heating rate of 100 °C/min, followed by cooling to the deformation temperatures (600, 700, 800 and 900 °C), and then deformed with the deformation reduction of 0.9 and the deformation rate of 0.1 s<sup>-1</sup>, before being finally cooled to room temperature with a cooling rate of 100 °C/min. For the deformation reduction experiments, the samples were also austenitized at 1000 °C for 10 min, followed by cooling to 900 °C and deformation with the different reductions (0.2, 0.5 and 0.9), and then cooled to room

temperature. For the deformation rate experiments, the samples were also deformed at 900 °C after austenitization, with the different deformation rates (0.01, 0.1 and 1 s<sup>-1</sup>).

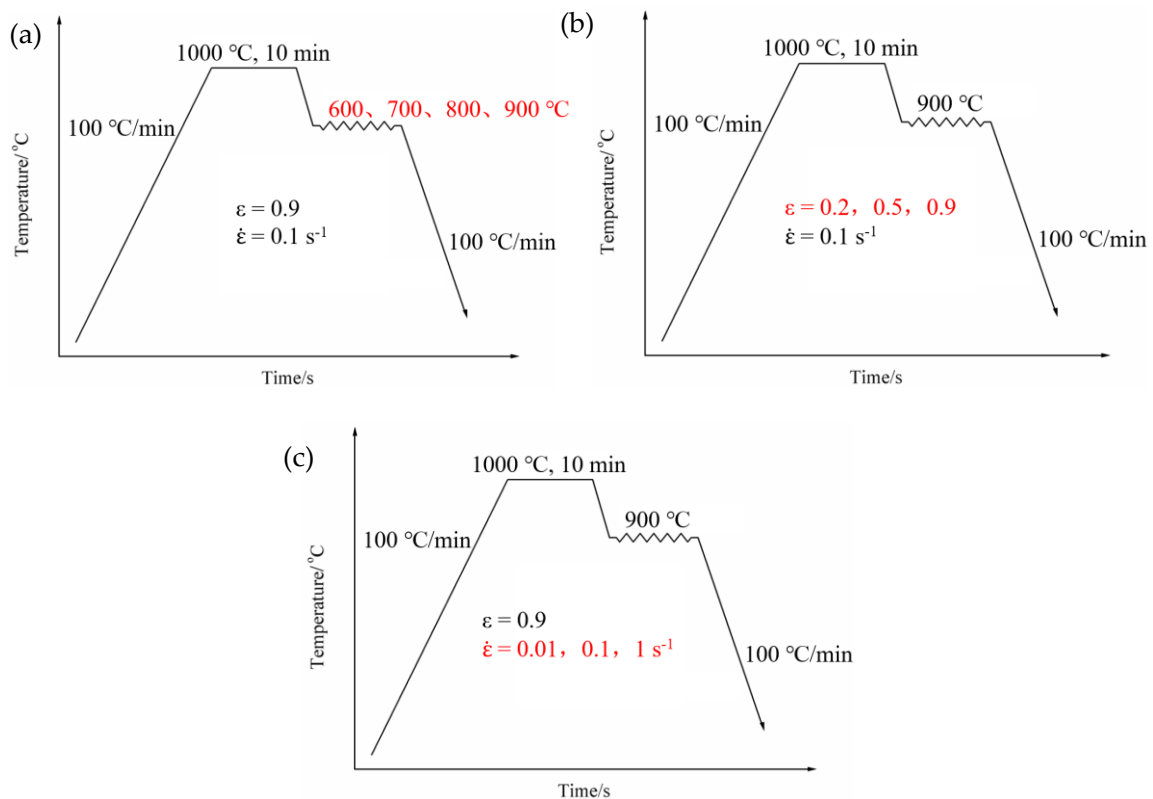


**Figure 2.** Schematic illustration of the different process parameters: (a) the different deformation temperatures, (b) the different deformation reductions, (c) the different deformation rates.

**Table 2.** The process parameters of the samples for the different conditions.

Experimental Conditions	Deformation Temperature/°C	Deformation Reduction	Deformation Rate/s <sup>-1</sup>
For the different deformation temperatures	600, 700, 800, 900	0.9	0.1
For the different deformation reductions	900	0.2, 0.5, 0.9	0.1
For the different deformation rates	900	0.9	0.01, 0.1, 1

After the deformation experiments, the samples were mounted, polished, and etched in a solution of hydrochloric acid (15 mL), ethanol (150 mL), and ferric chloride (5 g). The microstructures were observed by the C-35A OLYMPUS Optical Microscope (Tokyo, Japan). The stress–strain curves and the phase transformation points were captured by the accessory dilatometer of the Gleeble-3500 thermal simulated equipment (DSI, New York, NY, USA). The Vickers micro-hardness tests were carried out by the Duramin-A300 Vickers hardness tester (Struers, Ohio, OH, USA), with a load of 200 g and a pressure time of 10 s.

### 3. Results and Discussion

#### 3.1. Effect of the Deformation Temperature

As mentioned above, the original sample is in an as-rolled state, so the isothermal treatment at high temperature (annealing or normalizing) is necessary before deformation to remove the deformation texture and the residual stress caused by rolling. Figure 3 shows the equilibrium phase diagram of the employed low-carbon ferritic stainless steel calculated by JMatPro 7.0 software (Sente Software, Guildford, UK). It is found that, in the temperature range from 854 to 1068 °C, the steel is in the single-phase austenite region. Figure 4 gives the proof for the occurrence of austenitic transformation during heating with a rate of 100 °C/min. It can be seen that the inflection points resulted from austenitic transformation on the thermal expansion curve captured by Gleeble-3500. The  $A_{c1}$  and  $A_{c3}$  points can be determined as 837 and 991 °C. The transformation temperatures were determined from the dilatometer curves using the tangent line method [14].

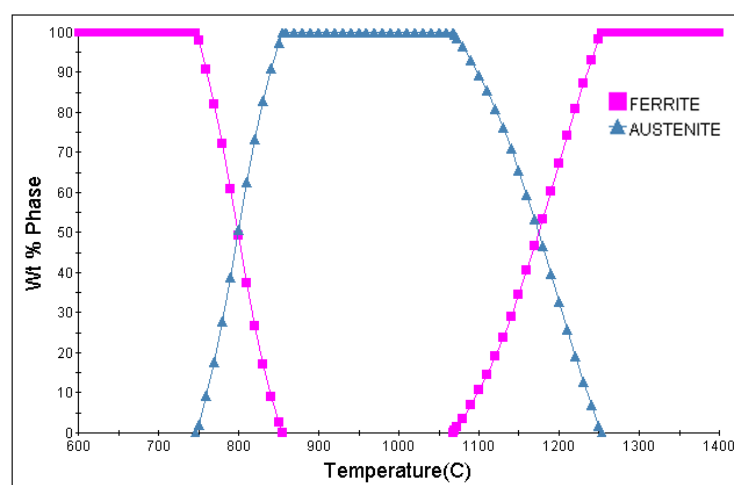


**Figure 3.** The equilibrium phase diagram of the employed low-carbon ferritic stainless steel calculated by JMatPro software.

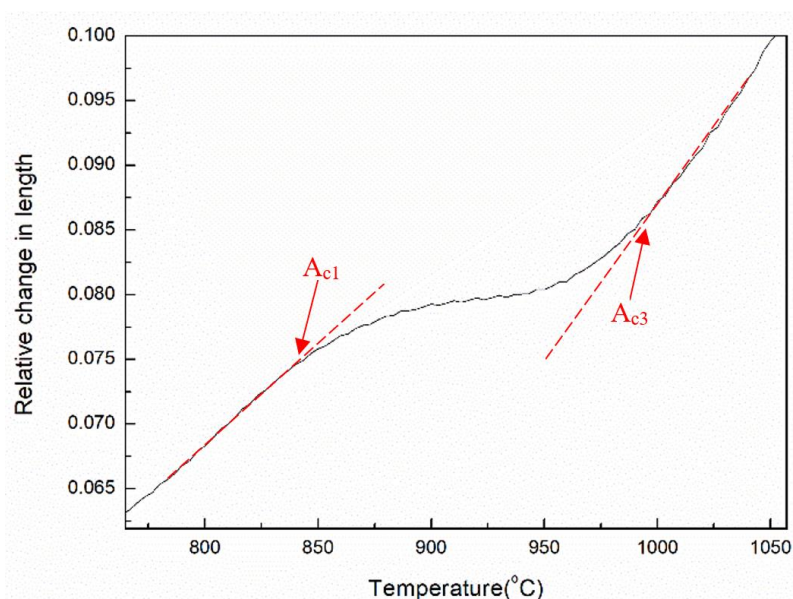


**Figure 4.** Thermal expansion curve of the low-carbon ferritic stainless steel sample during heating with a rate of 100 °C/min.

Figure 5 gives a continuous cooling transformation (CCT) diagram for the explored low-carbon ferritic stainless steel in this work, calculated by JMatPro software. It is found from Figure 5 that martensitic transformation occurs under the cooling rate between  $3\text{ }^{\circ}\text{C}/\text{min}$  ( $0.05\text{ }^{\circ}\text{C}/\text{s}$ ) and  $6000\text{ }^{\circ}\text{C}/\text{min}$  ( $100\text{ }^{\circ}\text{C}/\text{s}$ ). When the cooling rate is higher than  $18\text{ }^{\circ}\text{C}/\text{min}$  ( $0.3\text{ }^{\circ}\text{C}/\text{s}$ ), the ferritic transformation would not happen, and the austenite would be decomposed to martensite completely. According to the experimental CCT diagram for 3Cr12 steel [15], a typical low-carbon 12% Cr ferritic stainless steel, martensitic transformation still occurs when the cooling rate is as low as  $0.084\text{ }^{\circ}\text{C}/\text{min}$ . Figure 6 presents the microstructure of the low-carbon ferritic stainless steel sample after austenitization, whose treatment parameter is heating to  $1000\text{ }^{\circ}\text{C}$  with a heating rate of  $100\text{ }^{\circ}\text{C}/\text{min}$ , holding for 10 min, and cooling to room temperature with a cooling rate of  $100\text{ }^{\circ}\text{C}/\text{min}$ . Due to the moderate cooling rate after austenitization (air cooling), the bainitic and pearlite transformation would be avoided, and only martensite would form during cooling. As a result, it can be confirmed that the microstructure of the sample is composed of martensite (denoted as “M” in Figure 6), and  $\delta$ -ferrite distributed along the prior austenitic boundaries (denoted as “F” in Figure 6).

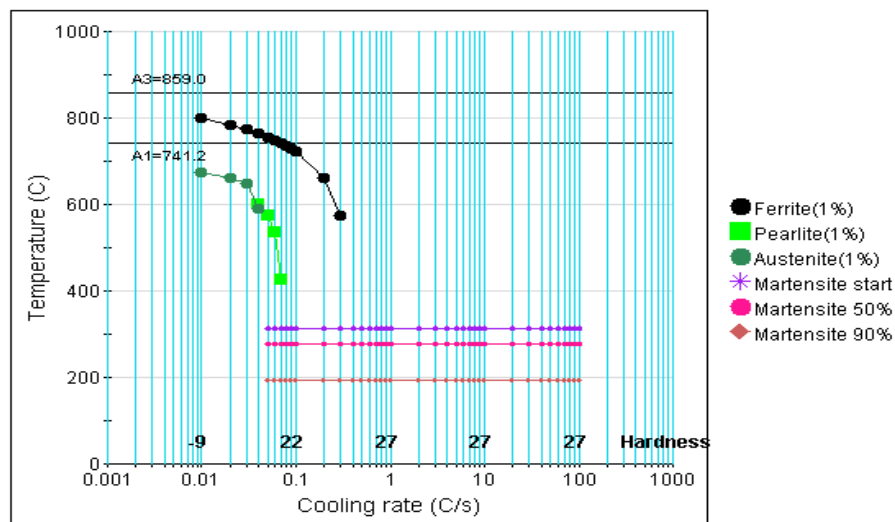


**Figure 5.** Continuous cooling transformation (CCT) diagram of the explored low-carbon ferritic stainless steel in this work calculated by JMatPro software.

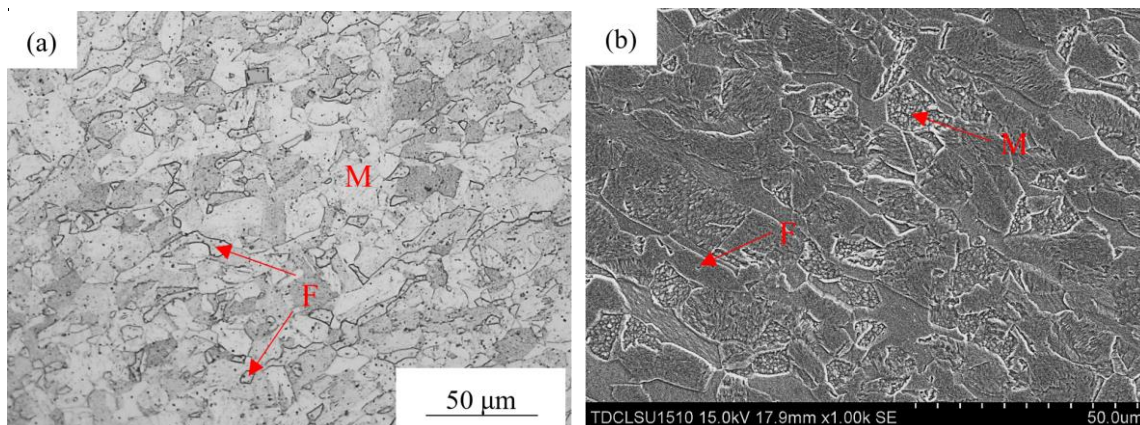


**Figure 6.** Microstructure of the low-carbon ferritic stainless steel sample after austenitization: (a) optical micrograph, (b) SEM micrograph.

A schematic illustration of the different deformation temperatures is given in Figure 2a. The deformation temperatures are  $600$ ,  $700$ ,  $800$  and  $900\text{ }^{\circ}\text{C}$ , respectively. Figure 7 presents the optical

micrographs of the low-carbon ferritic stainless steel samples deformed at the different temperatures. It is found that the microstructures of all samples are composed of ferrite and lath martensite. The sample with the deformation temperature of 600 °C shows the typical rolled microstructure, with the elongated grain morphology. This suggests that the deformation temperature of 600 °C is too low to cause dynamic recrystallization. On the other hand, the deformation texture with the elongated grain is not found in the microstructures of the samples deformed at 700, 800 and 900 °C, which are composed of the martensitic laths, and the fine equiaxed ferrite grain (with the diameter of about 5 μm) distributed among the martensitic laths. With the increase in deformation temperature, the amount of the fine equiaxed ferrite is increased, which results in the microstructures appearing finer in the samples deformed at the higher temperature.

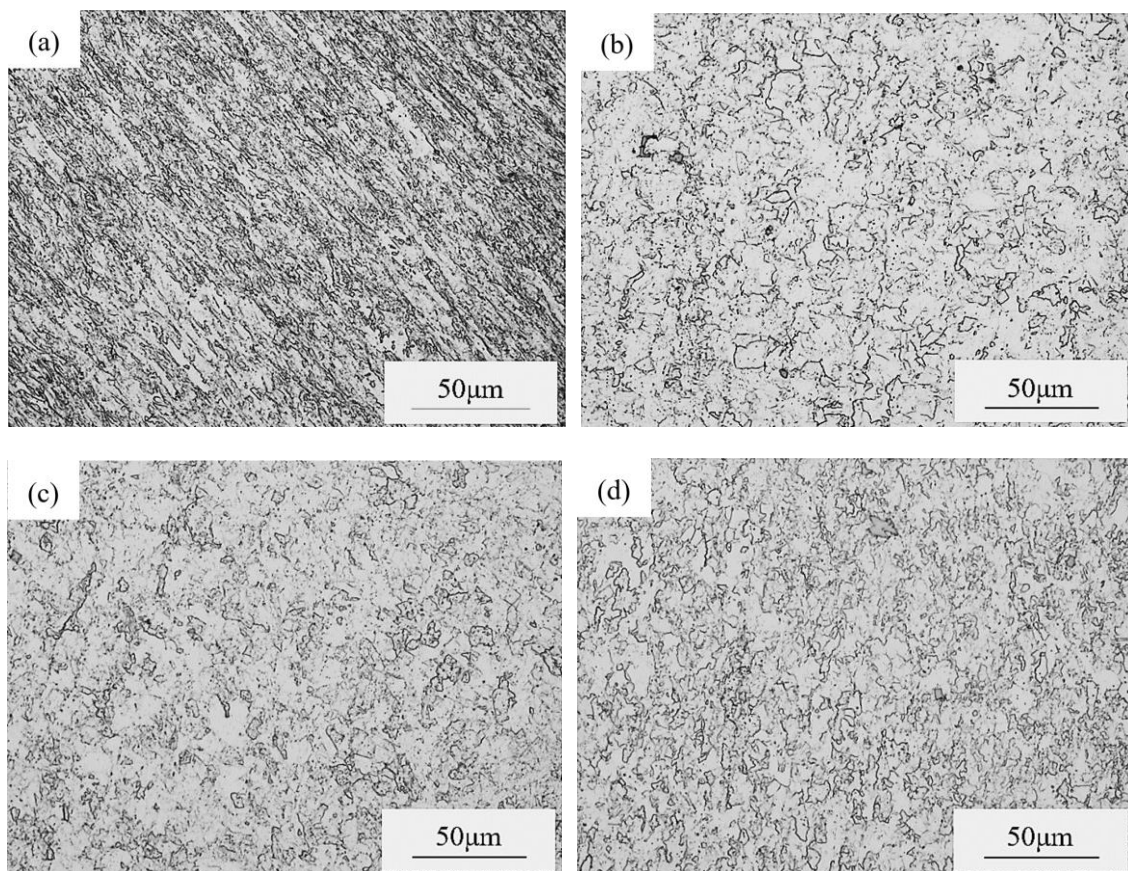


**Figure 7.** Optical micrographs of the low-carbon ferritic stainless steel samples deformed at the different temperatures: (a) 700 °C, (b) 800 °C, (c) 900 °C, (d) 1000 °C.

As discussed above, austenitic transformation occurs when heating up to 837 °C (namely  $A_{c1}$ ), and austenite transforms to lath martensite when the cooling rate is higher than 18 °C/min. Hence, it is recognized that the meta-stable austenite remains intact before deformation. During or after deformation, the austenite would be transformed to lath martensite or ferrite. Furthermore, it also found that the higher deformation temperature is favorable to the formation of fine equiaxed ferrite, while the lower deformation temperature promotes the formation of lath martensite. Generally speaking, a high temperature would result in a coarse grain [16]. However, this phenomenon was not observed in this project. This may be due to the dynamic transformation and recrystallization of ferrite during the high temperature deformation.

Figure 8 shows the phase transformation temperatures, determined by Gleeble-3500, for the low-carbon ferritic stainless steel samples deformed at the different temperatures. It can be confirmed as martensitic transformation, in consideration of the low transformation temperature. With the

increase in deformation temperature, the starting temperature for martensite transformation,  $M_s$ , is decreased, while the martensitic transformation finishing point remains almost unchanged, regardless of the deformation temperature. Besides, the  $M_s$  of the samples after deformation is higher than that of the samples without deformation (determined as 528 °C). This is because a large number of dislocations and other defects form during the deformation process, which provides more nucleation sites for martensitic transformation, and thus promotes martensitic transformation [17]. The higher the deformation temperature is, the more favorable the dynamic recovery of defects is. Hence, the number density of the defects is decreased accordingly, which results in a lower  $M_s$  in the sample with the higher deformation temperature.

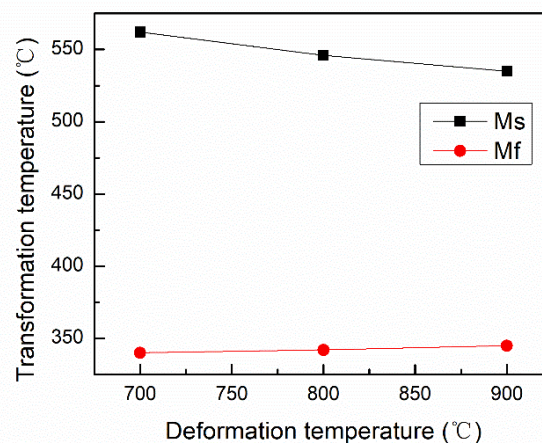


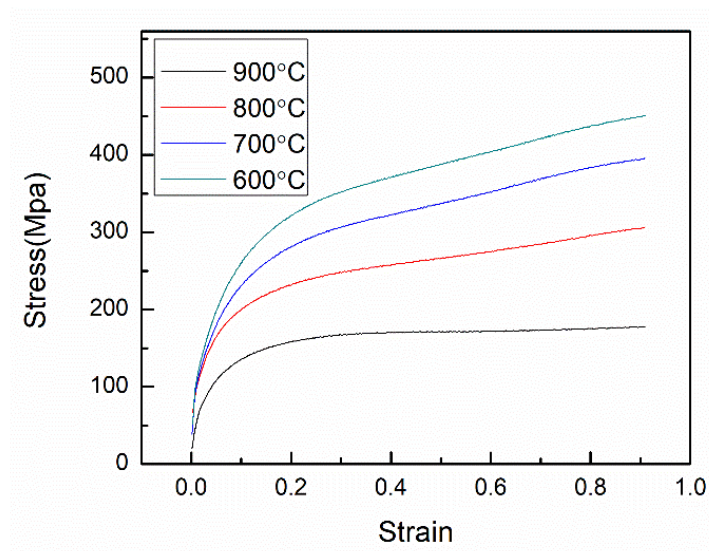
**Figure 8.** Phase transformation temperatures for the low-carbon ferritic stainless steel samples deformed at the different temperatures.

The formation of fine equiaxed ferrite was not detected in the thermal expansion curve determined by Gleeble-3500. This implies that ferritic transformation is likely to occur during the deformation process, rather than during continuous cooling after deformation. In general, this dynamic formation of fine ferrite during deformation is considered to be a dynamic strain-induced transformation (DSIT) [18]. When deformation is in the meta-stable austenite phase region, the dynamic strain-induced ferrite nucleates at the defects [19]. The movement of austenite-ferrite phase boundaries is hindered, due to the enhanced strength of the matrix caused by strain hardening, accompanied by dynamic recrystallization of ferrite grains. As a result, the DSIT ferrite grain size is very small.

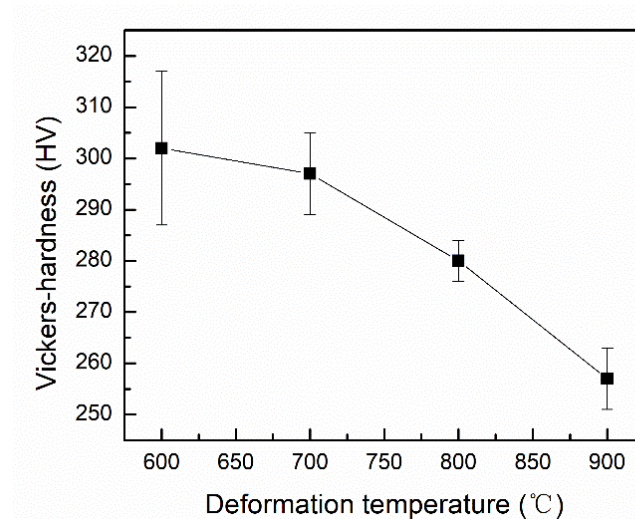
The stress–strain curves of the samples with the different deformation temperatures are presented in Figure 9. A decrease in deformation temperature leads to an increase in loading stress for reaching the same strain amount, since the yield strength of the steel is decreased by the increase in temperature. The stress–strain curves of the samples with the deformation temperatures of 600, 700 and 800 °C are monotonically increased, showing the typical characteristic of work hardening. On the other hand, in the sample deformed at 900 °C, when the strain is more than 0.3, the stress–strain curve is horizontal, representing the dynamic softening process [20]. Firstly, during deformation at high temperature, dynamic recovery and recrystallization occurs, offsetting the work hardening effect resulting from dislocation multiplication [21,22]. Secondly, according to the microstructural observation, the higher deformation temperature promotes the DSIT ferrite formation, accompanied by the movement and annihilation of dislocation, which also results in the loss of work hardening effect [19].

Figure 10 shows the values for Vickers hardness of the samples deformed at the different temperatures. It can be seen that the results of the hardness tests agree with the stress–strain curves. With the increase in deformation temperature, the hardness is decreased. This is mainly due to the fact that the rate of dynamic recovery and recrystallization will be faster when the sample is deformed at the higher temperature, which offsets the effect of work hardening. The difference in the phase

ratio of martensite to ferrite may also affect the hardness results. The size of the DSIT ferrite is higher up to about 5  $\mu\text{m}$  in this project, so the hardness of ferrite would be lower than that of lath martensite [23]. As mentioned above, the lower deformation temperature is more favorable to the formation of martensite, leading to the relatively high hardness. Besides, the residual stress remains at the lower deformation temperature, which may also lead to an increase in hardness.



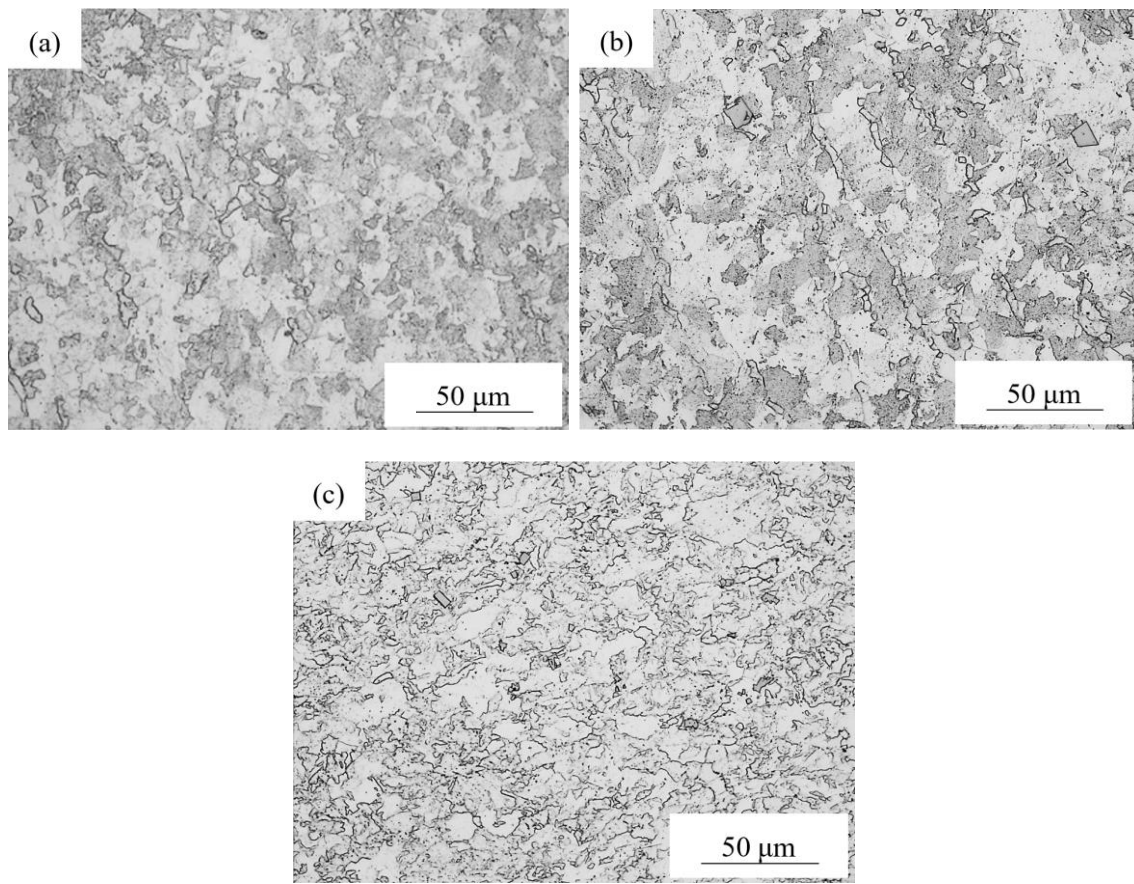
**Figure 9.** The true stress–strain curves for the low-carbon ferritic stainless steel samples deformed at the different temperatures.



**Figure 10.** Vickers hardness of the low-carbon ferritic stainless steel samples deformed at the different temperatures.

### 3.2. Effect of Deformation Reduction

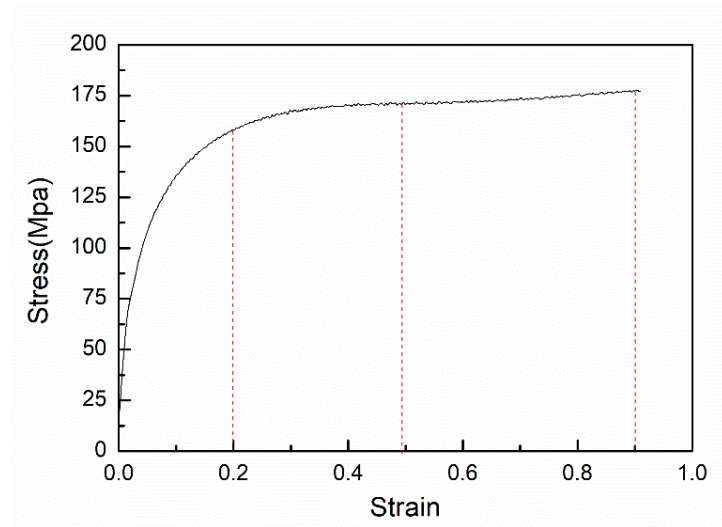
It can be recognized that the stress–strain curve for the sample deformed at 900 °C shows the feature of dynamic softening. Hence, the effect of deformation reduction was carried out at this temperature. A schematic illustration of the different deformation reductions is given in Figure 2b. Figure 11 presents the optical micrographs of the low-carbon ferritic stainless steel samples with the different deformation reductions. With the increase in deformation reduction, the fine equiaxed DSIT ferrite fraction is also increased. Obviously, a larger deformation reduction gives rise to more defects, and thus provides more nucleation sites for DSIT ferrite transformation.



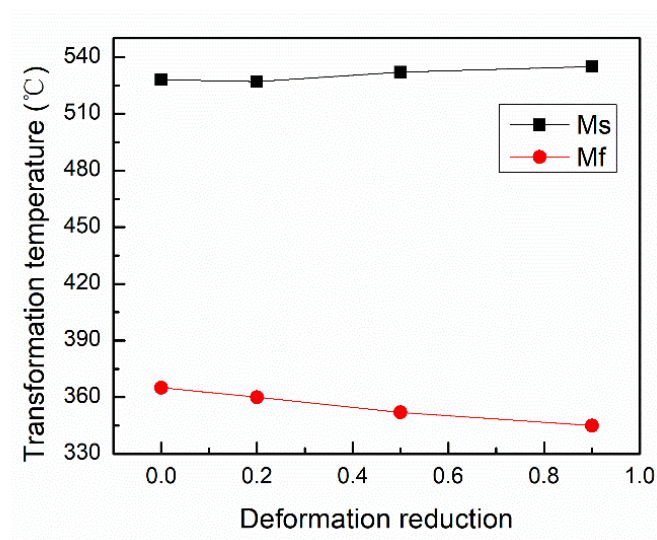
**Figure 11.** Optical micrographs of the low-carbon ferritic stainless steel samples with the different deformation reductions: (a) 0.2, (b) 0.5, (c) 0.9.

According to the stress–strain curve for the sample with the deformation reduction of 0.9 (Figure 12), before the deformation reduction reaches 0.2, the stress–strain curve belongs to the typical work hardening stage. In this stage, dislocation multiplication occurs with the increase in deformation. When the deformation reduction is between 0.2 and 0.5, the stress–strain curve steps into the stage of dynamic softening, including the dynamic recovery of dislocation and formation of DSIT ferrite. After the deformation reduction reaches 0.5, annihilation of dislocation and recrystallization of ferrite are dominant, resulting in the horizontal stress–strain curve.

Figure 13 presents the martensitic starting and finishing temperatures for the samples with the different deformation reductions. It is found that the  $M_s$  points are not significantly affected by the deformation reduction, but only slightly increased. Due to the high deformation temperature, the occurrence of recovery during cooling after deformation decreases the defect density, resulting in the decrease in nucleation sites for martensitic transformation accordingly. However, the  $M_f$  points are brought down by the increase in deformation reduction. This may be due to the fact that the movement of austenite/martensite phase boundaries is hindered during martensitic transformation. The martensitic transformation mechanism belongs to the non-diffusion type, with the shear-controlled phase transformation characteristics [24]. The yield strength of the parent phase (namely austenite) is improved by the increase in deformation reduction, impeding the migration of the martensite/austenite interface. Thus, the rate of martensitic transformation is decreased, reflected as the decrease in  $M_f$  points.



**Figure 12.** The true stress–strain curves for the low-carbon ferritic stainless steel samples with a deformation reduction of 0.9.



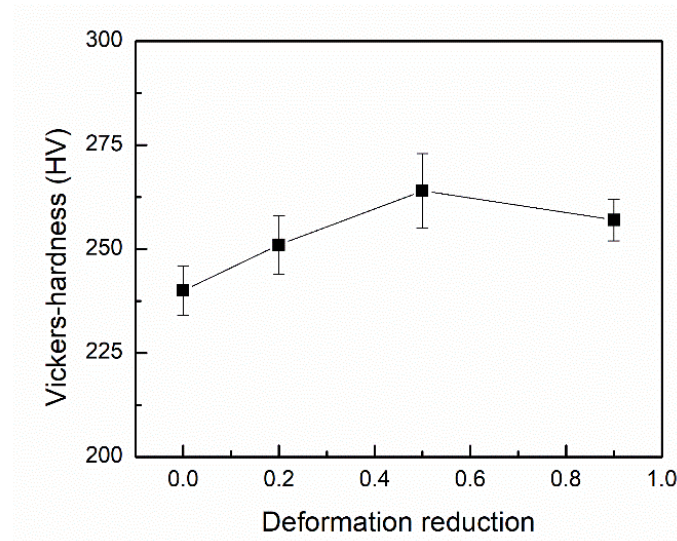
**Figure 13.** Phase transformation temperatures for the low-carbon ferritic stainless steel samples with the different deformation reductions.

Figure 14 shows the Vickers hardness of the samples with the different deformation reductions. The hardness values do not change greatly, though their general trend is to firstly increase and then decrease with the increase in deformation reduction. On the one hand, as discussed above, the hardness of lath martensite may be higher than that of ferrite. Therefore, with the increase in deformation reduction, the martensite fraction decreases, resulting in the decrease in hardness value. On the other hand, the increase in deformation increases the defect density, leading to the increase in strength and hardness. The combined effects of these two aspects result in a hardness value that does not monotonously increase or decrease with the increase in deformation reduction.

### 3.3. Effect of the Deformation Rate

A schematic illustration of the different deformation rates is given in Figure 2c. Figure 15 presents the optical micrographs of the samples with the different strain rates. It can be seen that the microstructures of all samples are composed of martensitic laths and fine ferrite grains. The increase in the strain rate leads to the increase in the phase fraction of ferrite and the decrease in lath

martensite fraction. There is not enough time for the recovery of dislocations and other defects at the high deformation rate, which provides more nucleation positions for DSIT ferrite and thus greatly promotes the ferrite transformation.



**Figure 14.** Vickers hardness of the low-carbon ferritic stainless steel samples with the different deformation reductions.

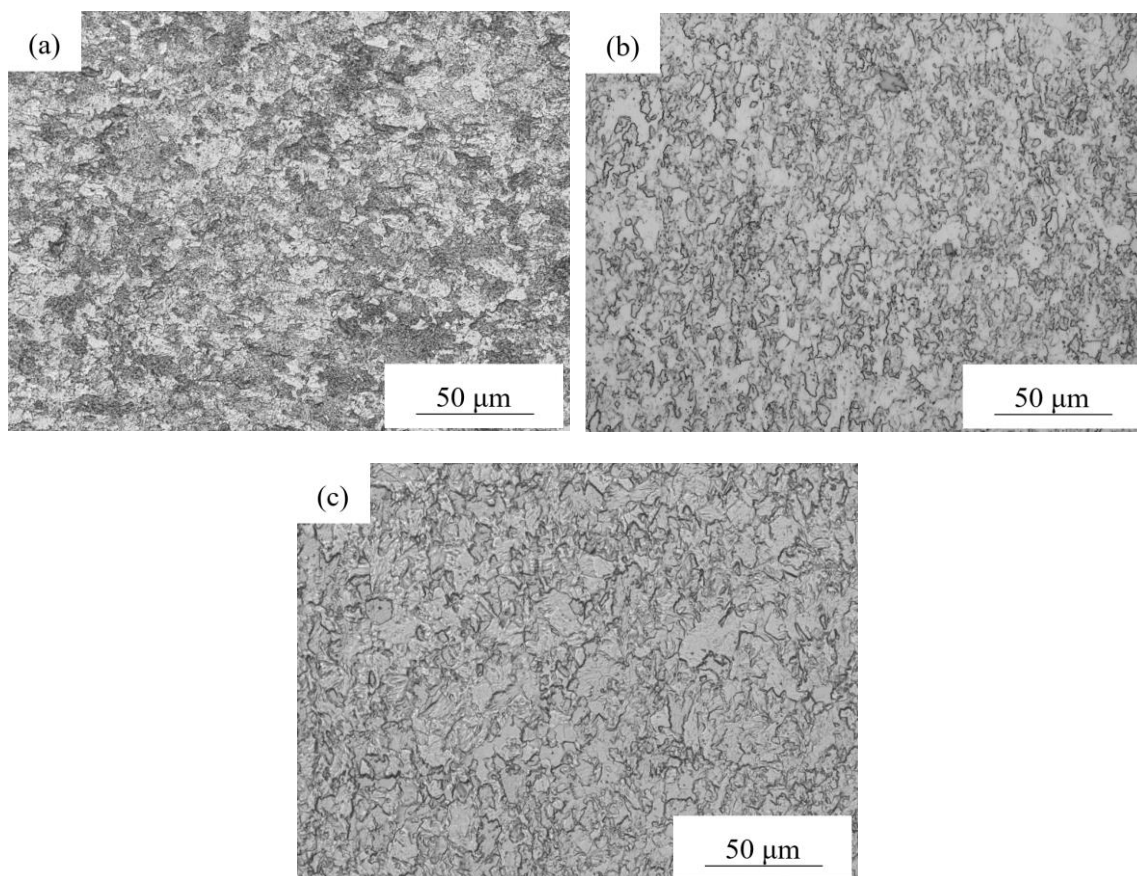


**Figure 15.** Optical micrographs of the low-carbon ferritic stainless steel samples with the different strain rates: (a)  $0.01 \text{ s}^{-1}$ , (b)  $0.1 \text{ s}^{-1}$ , (c)  $1 \text{ s}^{-1}$ .

The stress–strain curves for the different strain rates are shown in Figure 16. The stress–strain curve shows a more obvious softening with the decrease in the strain rate. The stress–strain curve of the sample undergoing the highest deformation rate ( $1 \text{ s}^{-1}$ ) reflects the typical work hardening characteristics. When the strain rate is the slowest ( $0.01 \text{ s}^{-1}$ ), the phase fraction of ferrite is the lowest. Thus, it is considered that the main origin of the softening phenomenon would be the dynamic recovery of dislocations, and the dynamic recrystallization of a small amount of ferrite grains.

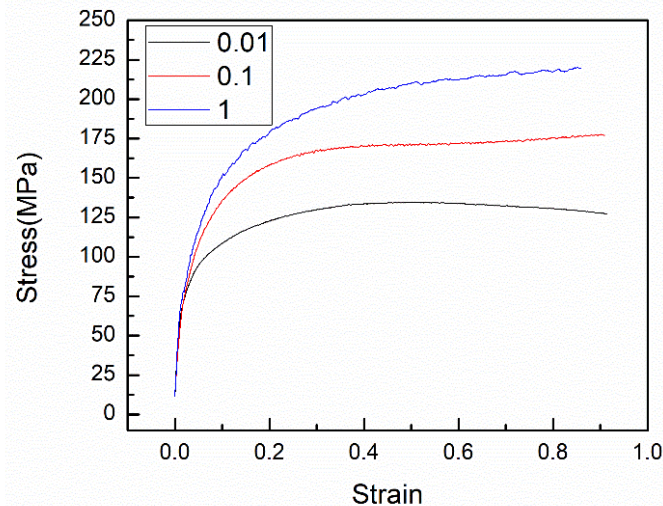


**Figure 16.** The true stress–strain curves for the low-carbon ferritic stainless steel samples with the different strain rates.

According to [25], the critical stress for recrystallization,  $\sigma_c$ , can be determined in the curves for the work-hardening rate,  $\theta$ , versus flow stress,  $\sigma$ , where  $\theta$  is expressed as  $d\sigma/d\varepsilon$ . As seen in Figure 17, the value for  $\sigma_c$  is associated with the point at which the second derivative of the work-hardening rate  $\theta$  with respect to stress, i.e.,  $d^2\theta/d\sigma^2$ , is zero. The simplest equation for fitting the  $\theta$ – $\sigma$  curve can be given by [26]:

$$\theta = A\sigma^3 + B\sigma^2 + C\sigma + D \quad (1)$$

where  $A$ ,  $B$ ,  $C$  and  $D$  are constants depending on the deformation parameters. Obviously, differentiation of the above equation with respect to  $\sigma$  is expressed as:

$$\frac{d\theta}{d\sigma} = 3A\sigma^2 + 2B\sigma + C \quad (2)$$

Thus, it can be derived that

$$\frac{d^2\theta}{d\sigma^2} = 6A\sigma + 2B \quad (3)$$

When  $d^2\theta/d\sigma^2 = 0$ ,  $\sigma_c$  can be obtained by

$$\sigma_c = -\frac{B}{3A} \quad (4)$$

For the sample deformed at  $900 \text{ }^\circ\text{C}$ , with a deformation rate of  $0.01 \text{ s}^{-1}$  the fitted polynomial is  $\theta = -0.01122\sigma^3 + 3.83996\sigma^2 - 443.62646\sigma + 17452.03963D$  (see Figure 1 below). Hence, the critical stress for recrystallization,  $\sigma_c$ , is calculated as  $114.08 \text{ MPa}$ . However,  $\sigma_c$  for all other samples is higher than the loading stresses. It should be noted that the sample in Figure 1 undergoes the highest deformation temperature and the slowest deformation rate. As the deformation temperature or the deformation rate is decreased, the dynamic recrystallization is blocked.

The martensitic starting and finishing temperatures for the samples with the different deformation rates are presented in Figure 18. It is found that an increase in the strain rate results in an increase in

$M_s$ . Under the condition of high strain rate, the high density of dislocation remains and provides more nucleation sites for the subsequent martensitic transformation, reflected as the increase in martensitic starting transformation temperature. Furthermore, the higher deformation rate results in a higher yield strength of the metastable austenite, which would hinder the movement of austenite/martensite boundaries during martensite. Hence, the increase in the deformation rate results in the decrease in the martensitic transformation rate, and thus the decrease in  $M_f$ .

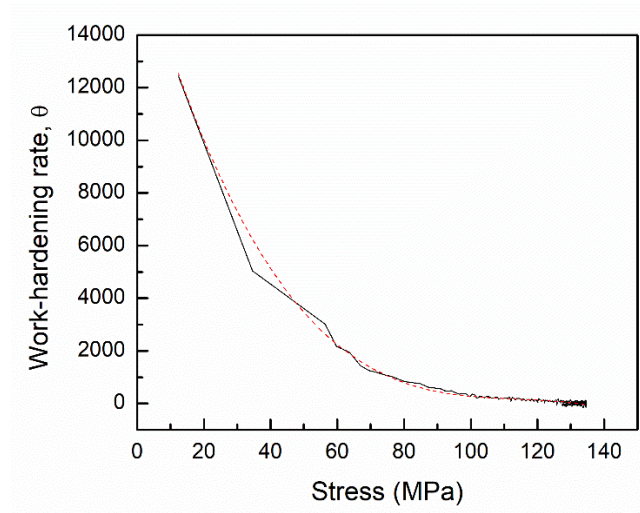


**Figure 17.** The experimental (black solid line) and fitted (red dashed line)  $\theta$ - $\sigma$  curves for the sample deformed at 900 °C, with a deformation rate of  $0.01 \text{ s}^{-1}$ .

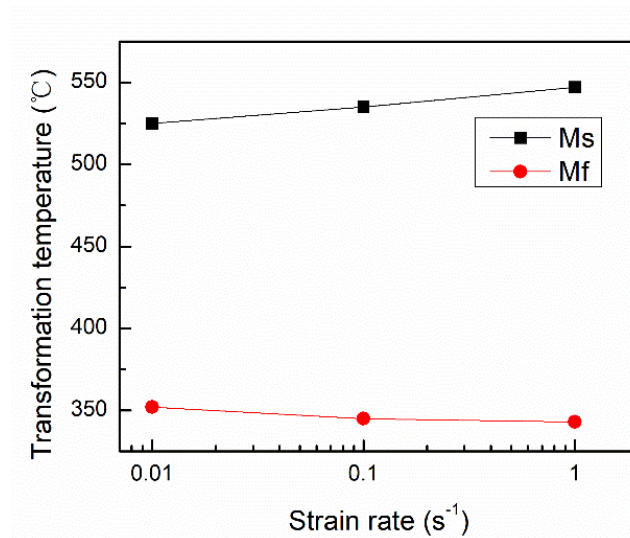


**Figure 18.** Phase transformation temperatures for the low-carbon ferritic stainless steel samples with the different strain rates.

Figure 19 shows the Vickers hardness of the samples with the different strain rates. With the increase in the strain rate, the hardness increases monotonically. This is attributed to the fact that the microstructure has sufficient time for recovery and recrystallization under the condition of slow strain rate, which leads to the reduction of hardness.

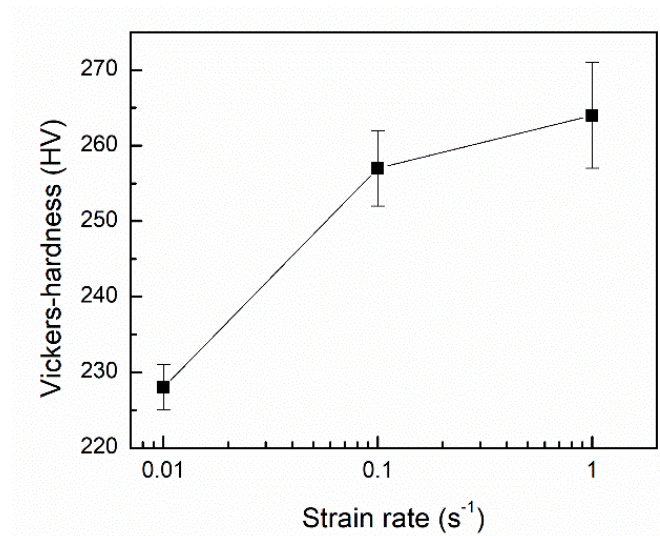


**Figure 19.** Vickers hardness of the low-carbon ferritic stainless steel samples with the different strain rates.

#### 4. Conclusions

In this paper, the effects of the deformation temperature, the deformation reduction and the deformation rate on the microstructures, phase transformation behaviors, stress–strain curves and mechanical properties were investigated. The main conclusions are as follows:

(1) The increase in deformation temperature promotes the formation of the fine equiaxed DSIT ferrite and suppresses the martensitic transformation. The higher deformation temperature results in a lower starting temperature for martensitic transformation. When the deformation temperature reaches 900 °C, the stress–strain curve shows an obvious softening phenomenon, and the hardness decreases to minimum.

(2) The increase in deformation can effectively promote the transformation of DSIT ferrite, and decrease the martensitic transformation rate, which is caused by the work hardening effect on the metastable austenite.

(3) The increase in the deformation rate leads to an increase in the ferrite fraction, because a high density of dislocation remains that can provide sufficient nucleation sites for ferrite transformation. The slow deformation rate results in dynamic recovery according to the stress–strain curve.

**Author Contributions:** Conceptualization, C.L.; methodology, Y.S. and J.M.; software, C.L.; validation, X.L.; formal analysis, Y.S.; investigation, Y.S. and J.M.; resources, C.L. and Z.Y.; data curation, X.L.; writing—original draft preparation, Y.S.; writing—review and editing, C.L.; supervision, C.L. and Z.Y.; project administration, X.L.; funding acquisition, C.L.

**Funding:** This research was funded by National Magnetic Confinement Fusion Energy Research Project, grant number 2015GB119001 and the Project of Natural Science Foundation of Tianjin, grant number 18JCQNJC03300 and 18YFZCGX00050.

**Conflicts of Interest:** The authors declare no conflict of interest.

#### References

1. Huh, M.Y.; Engler, O. Effect of intermediate annealing on texture, formability and ridging of 17%Cr ferritic stainless steel sheet. *Mater. Sci. Eng. A* **2001**, *308*, 74–87. [[CrossRef](#)]
2. Yan, H.; Bi, H.; Li, X.; Xu, Z. Microstructure and texture of Nb + Ti stabilized ferritic stainless steel. *Mater. Charact.* **2008**, *59*, 1741–1746. [[CrossRef](#)]

3. Seo, M.; Hultquist, G.; Leygraf, C.; Sato, N. The influence of minor alloying elements (Nb, Ti and Cu) on the corrosion resistivity of ferritic stainless steel in sulfuric acid solution. *Corros. Sci.* **1986**, *26*, 949–960. [[CrossRef](#)]
4. Mohandas, T.; Reddy, G.M.; Naveed, M. A comparative evaluation of gas tungsten and shielded metal arc welds of a “ferritic” stainless steel. *J. Mater. Process. Technol.* **1999**, *94*, 133–140. [[CrossRef](#)]
5. Wang, J.; Qian, S.; Li, Y.; Macdonald, D.D.; Jiang, Y.; Li, J. Passivity breakdown on 436 ferritic stainless steel in solutions containing chloride. *J. Mater. Sci. Technol.* **2019**, *35*, 637–643. [[CrossRef](#)]
6. Song, C.; Guo, Y.; Li, K.; Sun, F.; Han, Q.; Zhai, Q. In Situ Observation of Phase Transformation and Structure Evolution of a 12 pct Cr Ferritic Stainless Steel. *Metall. Mater. Trans. B* **2012**, *43*, 1127–1137. [[CrossRef](#)]
7. Shao, Y.; Liu, C.; Yue, T.; Liu, Y.; Yan, Z.; Li, H. Effects of Static Recrystallization and Precipitation on Mechanical Properties of 00Cr12 Ferritic Stainless Steel. *Metall. Mater. Trans. B* **2018**, *49*, 1560–1567. [[CrossRef](#)]
8. Fujita, N.; Ohmura, K.; Yamamoto, A. Changes of microstructures and high temperature properties during high temperature service of Niobium added ferritic stainless steels. *Mater. Sci. Eng. A* **2003**, *351*, 272–281. [[CrossRef](#)]
9. Hu, X.; Du, Y.; Yan, D.; Rong, L. Effect of Cu content on microstructure and properties of Fe-16Cr-2.5Mo damping alloy. *J. Mater. Sci. Technol.* **2018**, *34*, 774–781. [[CrossRef](#)]
10. Maki, T. Stainless steel: Progress in thermomechanical treatment. *Curr. Opin. Solid State Mater. Sci.* **1997**, *2*, 290–295. [[CrossRef](#)]
11. Sakai, T.; Belyakov, A.; Miura, H. Ultrafine Grain Formation in Ferritic Stainless Steel during Severe Plastic Deformation. *Metall. Mater. Trans. A* **2008**, *39*, 2206. [[CrossRef](#)]
12. Dobatkin, S.V. Severe Plastic Deformation of Steels: Structure, Properties and Techniques. In *Investigations and Applications of Severe Plastic Deformation*; Lowe, T.C., Valiev, R.Z., Eds.; Springer: Dordrecht, The Netherlands, 2000; pp. 13–22.
13. Belyakov, A.; Kaibyshev, R. Structural changes of ferritic stainless steel during severe plastic deformation. *Nanostruct. Mater.* **1995**, *6*, 893–896. [[CrossRef](#)]
14. Liu, C.; Liu, Y.; Zhang, D.; Yan, Z. Kinetics of isochronal austenization in modified high Cr ferritic heat-resistant steel. *Appl. Phys. A* **2011**, *105*, 949–957. [[CrossRef](#)]
15. van Warmelo, M.; Nolan, D.; Norrish, J. Mitigation of sensitisation effects in unstabilised 12%Cr ferritic stainless steel welds. *Mater. Sci. Eng. A* **2007**, *464*, 157–169. [[CrossRef](#)]
16. Wu, Y.; Liu, Y.; Li, C.; Xia, X.; Wu, J.; Li, H. Coarsening behavior of  $\gamma'$  precipitates in the  $\gamma' + \gamma$  area of a Ni3Al-based alloy. *J. Alloys Compd.* **2019**, *771*, 526–533. [[CrossRef](#)]
17. Liu, C.; Zhao, Q.; Liu, Y.; Wei, C.; Li, H. Microstructural evolution of high Cr ferrite/martensite steel after deformation in metastable austenite zone. *Fusion Eng. Des.* **2017**, *125*, 367–371. [[CrossRef](#)]
18. Zheng, C.; Xiao, N.; Hao, L.; Li, D.; Li, Y. Numerical simulation of dynamic strain-induced austenite–ferrite transformation in a low carbon steel. *Acta Mater.* **2009**, *57*, 2956–2968. [[CrossRef](#)]
19. Liu, Y.; Shao, Y.; Liu, C.; Chen, Y.; Zhang, D. Microstructure Evolution of HSLA Pipeline Steels after Hot Uniaxial Compression. *Materials* **2016**, *9*, 721. [[CrossRef](#)]
20. Dong, J.; Li, C.; Liu, C.; Huang, Y.; Yu, L.; Li, H.; Liu, Y. Hot deformation behavior and microstructural evolution of Nb–V–Ti microalloyed ultra-high strength steel. *J. Mater. Res.* **2017**, *32*, 3777–3787. [[CrossRef](#)]
21. Chen, J.; Liu, Y.; Liu, C.; Zhou, X.; Li, H. Study on microstructural evolution and constitutive modeling for hot deformation behavior of a low-carbon RAFM steel. *J. Mater. Res.* **2017**, *32*, 1376–1385. [[CrossRef](#)]
22. Zhou, Y.; Liu, Y.; Zhou, X.; Liu, C.; Yu, L.; Li, C.; Ning, B. Processing maps and microstructural evolution of the type 347H austenitic heat-resistant stainless steel. *J. Mater. Res.* **2015**, *30*, 2090–2100. [[CrossRef](#)]
23. Mao, C.; Liu, C.; Yu, L.; Li, H.; Liu, Y. The correlation among microstructural parameter and dynamic strain aging (DSA) in influencing the mechanical properties of a reduced activated ferritic-martensitic (RAFM) steel. *Mater. Sci. Eng. A* **2019**, *739*, 90–98. [[CrossRef](#)]
24. Tamura, I. Deformation-induced martensitic transformation and transformation-induced plasticity in steels. *Met. Sci.* **1982**, *16*, 245–253. [[CrossRef](#)]

25. Jonas, J.J.; Quelennec, X.; Jiang, L.; Martin, É. The Avrami kinetics of dynamic recrystallization. *Acta Mater.* **2009**, *57*, 2748–2756. [[CrossRef](#)]
26. Najafizadeh, A.; Jonas, J.J. Predicting the Critical Stress for Initiation of Dynamic Recrystallization. *ISIJ Int.* **2006**, *46*, 1679–1684. [[CrossRef](#)]



© 2019 by the authors. Licensee MDPI, Basel, Switzerland. This article is an open access article distributed under the terms and conditions of the Creative Commons Attribution (CC BY) license (<http://creativecommons.org/licenses/by/4.0/>).